

# Chemical models of interstellar glycine and adenine precursor aminoacetonitrile (NH<sub>2</sub>CH<sub>2</sub>CN)

Xia Zhang,<sup>1,2</sup> Donghui Quan,<sup>3,1</sup>★ Xiaohu Li,<sup>1,2,4</sup>† Jarken Esimbek,<sup>1,2,4</sup> Fangfang Li,<sup>1</sup> Yan Zhou<sup>5</sup> and Dalei Li<sup>1,2,4</sup>

<sup>1</sup> Xijiang Astronomical Observatory, Chinese Academy of Sciences, 150 Science 1-Street, Urumqi, Xinjiang 830011, China

<sup>2</sup> Xijiang Key Laboratory of Radio Astrophysics, 150 Science 1-Street, Urumqi 830011, China

<sup>3</sup> Research Center for Astronomical Computing, Zhejiang Laboratory, Hangzhou 311100, China

<sup>4</sup> Key Laboratory of Radio Astronomy, Chinese Academy of Sciences, Nanjing 210008, China

<sup>5</sup> Binzhou University, Huanghe Road, Binzhou City, Shandong, 256600, China

Accepted XXX. Received YYY; in original form ZZZ

## ABSTRACT

Aminoacetonitrile (AAN), also known as glycinenitrile, has been suggested as a possible precursor of glycine and adenine in the interstellar medium. Here we present the chemical modeling of AAN and its isomers in hot cores using the three-phase chemical model NAUTILUS with the addition of over 300 chemical reactions of the three AAN isomers and related species. Our models predicted a peak gas phase abundance of AAN reaching the order of  $10^{-8}$ , which is consistent with observation towards Sgr B2(N). Regarding the reaction pathways of AAN and its isomers, we found that AAN is primarily formed via free radical reactions on grain surfaces during the early evolutionary stages. Subsequently, it is thermally desorbed into the gas phase as the temperature rises and is then destroyed by positive ions and radicals in gas phase. The isomers of AAN are formed through the hydrogenation reaction of CH<sub>3</sub>NCN on the grain surface and via electron recombination reactions of ion C<sub>2</sub>H<sub>5</sub>N<sub>2</sub><sup>+</sup> in gas phase. We speculate that there is a possibility for NCCN and AAN to react with each other, eventually leading to the formation of adenine in hot cores. However, further investigation is required to understand the efficiency of grain surfaces in adenine formation, through theoretical calculations or laboratory experiments in future research.

**Key words:** astrochemistry – molecular processes – ISM: abundances – ISM: molecules.

## 1 INTRODUCTION

Amino acids, which are the building blocks of proteins and therefore essential for understanding the origin of life, have been discovered in meteorites and comets (Glavin et al. 2010; Elsila et al. 2009). Therefore, it is intriguing to search for amino acids in the interstellar medium (ISM). However, despite a 40-year search, even the simplest amino acid, glycine, has not yet been detected. Aminoacetonitrile (AAN), also known as glycinenitrile, has been proposed as a potential precursor of glycine in the ISM. AAN can form glycine by Strecker synthesis, in which water reacts with a nitrile to form the corresponding acid (Peltzer et al. 1984). Choe (2023) found AAN can form glycine through a barrierless pathway from the reaction of AAN + OH + H<sub>2</sub>O with H<sub>2</sub>O as a catalyst by theoretical calculation and they suggest the reaction can occur on icy grain surfaces in the ISM. Vasconcelos et al. (2020) proposed a plausible mechanism for the formation of adenine (C<sub>5</sub>H<sub>5</sub>N<sub>5</sub>), one of the purine of DNA and RNA nucleobases. According to their proposal, AAN may react with cyanogen (NCCN), forming diaminomaleonitrile (C<sub>4</sub>H<sub>4</sub>N<sub>4</sub>), and then C<sub>4</sub>H<sub>4</sub>N<sub>4</sub> reacts with HCN to produce adenine.

Wirström et al. (2007) firstly attempted to detect AAN towards four northern hot core sources Orion KL, W51 e1/e2, W3(OH) and

S140 using the Onsala 20 m telescope and suggested upper limits to the column density of AAN ( $1 - 4 \times 10^{13} \text{cm}^{-2}$ ). Later, Belloche et al. (2008) successfully detected AAN towards Sgr B2(N) regions using the IRAM 30 m telescope. They speculated that the column density of AAN was  $2.8 \times 10^{16} \text{cm}^{-2}$  at the temperature of 100 K. In Sgr B2(M) region, they derived an upper limit of  $6 \times 10^{15} \text{cm}^{-2}$ . Richard et al. (2018) detected AAN towards Sgr B2(N2) hot core in the EMoCA (Exploring Molecular Complexity with ALMA) survey. They derived a column density of  $9.7 \times 10^{16} \text{cm}^{-2}$  at a rotational temperature of 150 K for AAN. Additionally, Richard et al. (2018) also tentatively detected aminopropionitrile (APN), the family of AAN, which is the next stage in complexity with one additional CH<sub>2</sub> group comparing to AAN. The molecule has two structural isomers, 3-aminopropionitrile (NH<sub>2</sub>CH<sub>2</sub>CH<sub>2</sub>CN) and 2-aminopropionitrile (CH<sub>3</sub>CH(NH<sub>2</sub>)CN). However, neither 3-aminopropionitrile nor 2-aminopropionitrile was detected. Recently, Melosso et al. (2020) used the imaging spectral line survey ReMoCA (Re-exploring Molecular Complexity with ALMA) to search AAN towards Sgr B2(N1) and derived a column density of  $1.1 \times 10^{17} \text{cm}^{-2}$  at a rotational temperature of 200 K. Besides, AAN was also tentatively detected in the hot molecular core G10.47+0.03 using ALMA data (Manna & Pal 2022; Mondal et al. 2023).

AAN is one of nitriles that have been found to exhibit greater stability than glycine acids when exposed to UV photolysis in the solid

★ E-mail: donghui.quan@zhejianglab.com

† E-mail: xiaohu.li@xao.ac.cn

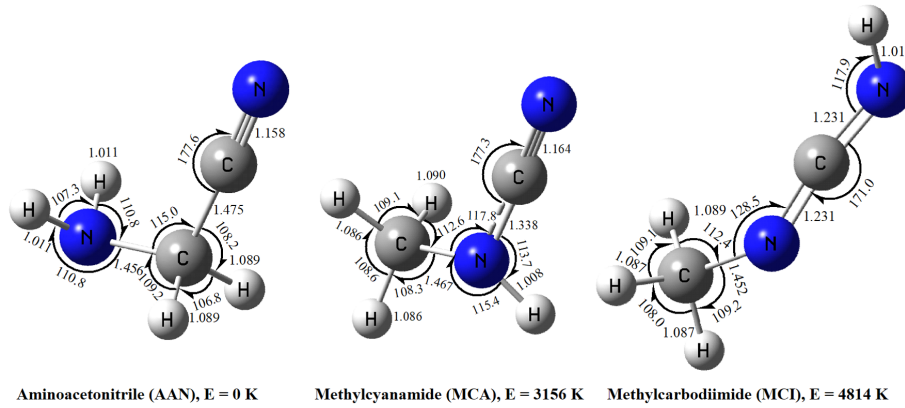


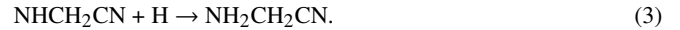
**Figure 1.** Optimized structures of the three isomers. Energies have been calculated at the CCSD(T)/aug-cc-pVTZ//B2PLYPD3/may-cc-pVTZ level. Blue, gray, white spheres correspond to nitrogen, carbon, and hydrogen atoms, respectively.

state at 15 K, according to experiments conducted by [Bernstein et al. \(2004\)](#). These findings suggest that nitriles may be more abundant than acids in the ISM, in part due to their slower destruction through photolysis. [Pelc et al. \(2016\)](#) concluded that AAN was less susceptible to electron capture through low anion yields using experiments and quantum chemical calculations. Therefore, AAN can be considered to exhibit a relatively long lifetime under typical conditions in ISM.

According to [Lattelais et al. \(2010\)](#),  $C_2H_4N_2$  has seventeen structures. AAN is the most stable structure, followed by methylcyanamide ( $CH_3NHCN$ , MCA) and methylcarbodiimide ( $CH_3NCNH$ , MCI). The structural images of three isomers are shown in Fig. 1. Among them, MCA and MCI, have not been studied extensively nor been discovered in the ISM ([Bak 1980](#); [Sleiman et al. 2018](#); [Wang et al. 2019](#)). It is worth noting that both MCA and MCI are chiral molecules, meaning that they both have mirror image molecules. Many life-related molecules are chiral, such as amino acids and sugar, where amino acids are always left-handed, and sugars are always right-handed. The first interstellar chiral molecule, propylene oxide ( $CH_3CHOCH_2$ ), was discovered in the star formation region Sgr B2 ([McGuire et al. 2016](#)). This finding suggests that the chiral molecules essential for life may have originated from space, particularly from star-forming regions. Furthermore, MCA may undergo hydrolysis, similar to AAN, resulting in the formation of methylcarbamic acid ( $CH_3NHCOOH$ ) acid. This acid is an isomer of glycine and is considered the most stable structure ([Lattelais et al. 2011](#)).

There are multiple pathways to form AAN. The reaction between methanimine ( $CH_2NH$ ) and HCN (or HNC) was proposed both in gas phase and on surface by [Xu & Wang \(2007\)](#) and [Koch et al. \(2008\)](#) based on theoretical calculation. They discovered that this pathway in the gas phase exhibits significant barriers, whereas they appear to be feasible on the grain surface.

[Belloche et al. \(2009\)](#) proposed two grain-phase reactions related to AAN. These reactions involve the interaction between CN and  $CH_2NH$ , as well as reaction between NH and cyanomethyl radical ( $H_2CCN$ ). Both of them firstly produce  $NHCH_2CN$ , which subsequently reacts with atomic H to produce AAN, as follows:



[Belloche et al. \(2009\)](#) also proposed two direct routes to form AAN on the grain surface, they are as follows:



Later, [Danger et al. \(2011\)](#) demonstrated that AAN can be formed at 20 K from the Vacuum Ultraviolet (VUV) irradiation of acetonitrile ( $CH_3CN$ ) with the presence of ammonia using experimental investigation, which can produce the radicals  $H_2CCN$  and  $NH_2$ . Then Reaction (5) subsequently occurs to produce AAN. The reaction between CN and methylamine ( $CH_3NH_2$ ) can form AAN, but it has a relatively high barrier ([Sleiman et al. 2018](#); [Puzzarini et al. 2020](#)).

For isomeric MCA, [Sleiman et al. \(2018\)](#) proposed that the reaction between CN +  $CH_3NH_2$  can form MCA using experimental and theoretical simulations at temperatures ranging from 23 to 297 K, which represents the second most significant channel among three. However, [Puzzarini et al. \(2020\)](#) found there is high energy barrier by quantum-chemical study.

So far, three research groups have reported modeling of interstellar AAN ([Belloche et al. 2009](#); [Garrod 2013](#); [Mondal et al. 2023](#)). [Belloche et al. \(2009\)](#) modeled the chemistry of Sgr B2(N) using gas-grain-mantel three phase code with addition of reactions of ethyl format, ethyl, n-propyl cyanide and AAN. Later, [Garrod \(2013\)](#) used a three-phase model of hot cores to model the formation of glycine, which included the chemistry of AAN from [Belloche et al. \(2009\)](#). [Garrod \(2013\)](#) found that the major formation of AAN is the reaction between  $NH_2$  and  $H_2CCN$  (Reaction (5)) and also derived the formation of AAN associated with the thermal desorption of  $CH_3CN$ , which can produce the radical  $H_2CCN$  through the gas phase destruction routes. The  $H_2CCN$  could re-accrete onto the grains and react with  $NH_2$  to form AAN. The two studies both produced fractional abundances of AAN on the order of  $10^{-8}$ . [Mondal et al. \(2023\)](#) also used a three-phase version of NAUTILUS gas-grain code to simulate some nitrogen-bearing complex organic molecules in the hot molecular core, G10.47+0.03. Their chemical network of AAN is based on [Belloche et al. \(2009\)](#). However, these studies did not focus on AAN. So the reactions presented may be incomplete. Additionally, the isomers of AAN were not considered. Therefore, more comprehensive studies are needed to better understand AAN as well as its isomers.

In this study, we consider reactions that have been experimentally approved or theoretically suggested for AAN, MCA, and MCI. Additionally, we also propose new reactive routes which are calculated by quantum chemistry calculations, and present them in Section 2. In Section 3, we show chemical kinetics models that are developed to simulate the formation and destruction mechanisms of the three prebiotic molecules under the interstellar physical conditions. We also explore the possible interstellar environment for further formation of these molecules. Moreover, we conducted an investigation and analysis of the modeling results for cyanamide ( $\text{NH}_2\text{CN}$ ), methylenimine ( $\text{CH}_2\text{NH}$ ), methylamine ( $\text{CH}_3\text{NH}_2$ ), cyanomethyl radical ( $\text{H}_2\text{CCN}$ ), acetonitrile ( $\text{CH}_3\text{CN}$ ) and cyanogen ( $\text{NCCN}$ ) and discuss the results in Section 4. Finally, we draw conclusions and summarize our findings in Section 5.

## 2 CHEMISTRY OF AAN, MCA AND MCI

### 2.1 Formation and destruction of AAN, MCA and MCI

In addition to the previously mentioned chemical reactions of AAN, we expanded our investigation to include other types of reactions involving AAN, as well as reactions concerning MCA and MCI. The major types of reactions considered in this study include cosmic-ray induced photodissociation, UV photodissociation, dissociative recombination, ion-neutral and neutral-neutral reactions. For the first three types of reactions, rate parameters are estimated based on similar reactions already existing in the chemical network. For ion-molecule reactions, since the branching ratios to these different channels are frequently unmeasured, we assume that reactions proceed equally through different channels, i.e., the branching ratios adopt the same value. And the corresponding rate parameters are calculated using the method developed by Woon & Herbst (2009). For neutral-neutral reactions, quantum chemical calculations were performed to select only barrierless or lower-barrier exothermic reactions as the possible efficient formation reactions, whose rate coefficients were calculated by the modified Arrhenius equation. The activation energies of the destruction reactions of AAN, by OH,  $\text{NH}_2$ ,  $\text{CH}_2\text{OH}$ , and  $\text{CH}_3\text{O}$ , were estimated based on analogous reactions outlined in Garrod (2013). We then performed quantum chemical calculations to obtain accurate values. Additionally, we also added the destruction of MCA and MCI by the four radicals listed above. Tables 1 and 2 present the rate coefficients for gas-phase reactions of AAN, MCA, MCI, and related species, as well as the activation energy barriers for surface/mantle reactions. Moreover, Table 3 provides the binding energies of selected species utilized in the models. Fig. 2 presents the neutral-neutral reactions linking AAN and its isomers, using the color code indicating the isomers. In addition, blue arrows represent hydrolysis reactions or the reaction among AAN, OH and  $\text{H}_2\text{O}$ . Green arrows denote the reactions for the formation of glycine and its isomer on the grain surface, purple and dark purple arrows and corresponding species represent reactions that need to be clarified by theoretical and experimental studies. The reaction pathways of glycine and its isomer,  $\text{C}_4\text{H}_4\text{N}_4$  and adenine are currently not included in this work.

### 2.2 Quantum chemical calculations

All quantum chemical calculations were performed using the GAUSSIAN 16 program (Frisch et al. 2016). The structures of the reactants, transition states, intermediates, and products were optimized,

and zero-point energy corrections were determined using the double-hybrid B2PLYP functions (Grimme 2006) with the *may-cc-pVTZ* basis set. Semi-empirical dispersion contributions were also included by using the D3BJ model (Goerigk & Grimme 2011; Grimme et al. 2011). Single-point energies were then calculated using the highly cost-effective method of CCSD(T) (Purvis III & Bartlett 1982; Scuseria et al. 1988; Scuseria & Schaefer III 1989), together with the basis set of *aug-cc-pVTZ*. Saddle points were assigned to reaction paths by using the intrinsic reaction coordinate (IRC) (Fukui 1981) calculations at the same B2PLYP level as the identification of reactants and products.

Table 1: Summary of the rate coefficients of gas-phase reactions involving AAN, MCA, MCI and related species.

Reaction	$\alpha$	$\beta$	$\gamma$	Ref.
<b>Cosmic Ray Induced Photodissociation</b>				
	(-)	(-)	(-)	
$\text{NH}_2\text{CH}_2\text{CN} \rightarrow \text{NH}_2 + \text{H}_2\text{CCN}$	1.50E+03	0	0	a
$\text{NH}_2\text{CH}_2\text{CN} \rightarrow \text{CH}_2\text{NH}_2 + \text{CN}$	1.50E+03	0	0	a
$\text{NH}_2\text{CH}_2\text{CN} \rightarrow \text{NH}_2\text{CHCN} + \text{H}$	1.50E+03	0	0	a
$\text{NH}_2\text{CH}_2\text{CN} \rightarrow \text{NHCH}_2\text{CN} + \text{H}$	1.50E+03	0	0	a
$\text{NHCH}_2\text{CN} \rightarrow \text{H}_2\text{CCN} + \text{NH}$	1.50E+03	0	0	a
$\text{NHCH}_2\text{CN} \rightarrow \text{CH}_2\text{NH} + \text{CN}$	1.50E+03	0	0	a
$\text{NH}_2\text{CHCN} \rightarrow \text{HCCN} + \text{NH}_2$	1.50E+03	0	0	a
$\text{NH}_2\text{CHCN} \rightarrow \text{CH}_2\text{NH} + \text{CN}$	1.50E+03	0	0	a
$\text{CH}_3\text{NHCN} \rightarrow \text{CH}_3\text{NH} + \text{CN}$	1.50E+03	0	0	a
$\text{CH}_3\text{NHCN} \rightarrow \text{CH}_3 + \text{HNCN}$	1.50E+03	0	0	a
$\text{CH}_3\text{NHCN} \rightarrow \text{CH}_3\text{NCN} + \text{H}$	1.50E+03	0	0	a
$\text{CH}_3\text{NHCN} \rightarrow \text{CH}_2\text{NHCN} + \text{H}$	1.50E+03	0	0	a
$\text{CH}_3\text{NCNH} \rightarrow \text{CH}_3 + \text{HNCN}$	1.50E+03	0	0	a
$\text{CH}_3\text{NCNH} \rightarrow \text{CH}_3\text{NCN} + \text{H}$	1.50E+03	0	0	a
$\text{CH}_3\text{NCNH} \rightarrow \text{CH}_2\text{NCNH} + \text{H}$	1.50E+03	0	0	a
$\text{CH}_3\text{NCN} \rightarrow \text{CH}_3 + \text{NCN}$	1.50E+03	0	0	a
$\text{CH}_2\text{NCNH} \rightarrow \text{CH}_2 + \text{HNCN}$	1.50E+03	0	0	a
$\text{CH}_2\text{NHCN} \rightarrow \text{CH}_2 + \text{HNCN}$	1.50E+03	0	0	a
$\text{CH}_2\text{NHCN} \rightarrow \text{CH}_2\text{NH} + \text{CN}$	1.50E+03	0	0	a
$\text{CH}_3\text{NH} \rightarrow \text{CH}_2\text{NH} + \text{H}$	1.50E+03	0	0	a
$\text{CH}_3\text{NH} \rightarrow \text{CH}_3 + \text{NH}$	1.50E+03	0	0	a
<b>Photodissociation</b>				
	( $s^{-1}$ )	(-)	(-)	
$\text{NH}_2\text{CH}_2\text{CN} \rightarrow \text{NH}_2 + \text{H}_2\text{CCN}$	1.00E-09	0	1.9	a
$\text{NH}_2\text{CH}_2\text{CN} \rightarrow \text{CH}_2\text{NH}_2 + \text{CN}$	1.00E-09	0	1.9	a
$\text{NH}_2\text{CH}_2\text{CN} \rightarrow \text{NH}_2\text{CHCN} + \text{H}$	1.00E-09	0	1.9	a
$\text{NH}_2\text{CH}_2\text{CN} \rightarrow \text{NHCH}_2\text{CN} + \text{H}$	1.00E-09	0	1.9	a
$\text{NHCH}_2\text{CN} \rightarrow \text{H}_2\text{CCN} + \text{NH}$	1.00E-09	0	1.9	a
$\text{NHCH}_2\text{CN} \rightarrow \text{CH}_2\text{NH} + \text{CN}$	1.00E-09	0	1.9	a
$\text{NH}_2\text{CHCN} \rightarrow \text{HCCN} + \text{NH}_2$	1.00E-09	0	1.9	a
$\text{NH}_2\text{CHCN} \rightarrow \text{CH}_2\text{NH} + \text{CN}$	1.00E-09	0	1.9	a
$\text{CH}_3\text{NHCN} \rightarrow \text{CH}_3\text{NH} + \text{CN}$	1.00E-09	0	1.9	a
$\text{CH}_3\text{NHCN} \rightarrow \text{CH}_3 + \text{HNCN}$	1.00E-09	0	1.9	a
$\text{CH}_3\text{NHCN} \rightarrow \text{CH}_3\text{NCN} + \text{H}$	1.00E-09	0	1.9	a
$\text{CH}_3\text{NHCN} \rightarrow \text{CH}_2\text{NHCN} + \text{H}$	1.00E-09	0	1.9	a
$\text{CH}_3\text{NCNH} \rightarrow \text{CH}_3 + \text{HNCN}$	1.00E-09	0	1.9	a
$\text{CH}_3\text{NCNH} \rightarrow \text{CH}_3\text{NCN} + \text{H}$	1.00E-09	0	1.9	a
$\text{CH}_3\text{NCNH} \rightarrow \text{CH}_2\text{NCNH} + \text{H}$	1.00E-09	0	1.9	a
$\text{CH}_3\text{NCN} \rightarrow \text{CH}_3 + \text{NCN}$	1.00E-09	0	1.9	a
$\text{CH}_2\text{NCNH} \rightarrow \text{CH}_2 + \text{HNCN}$	1.00E-09	0	1.9	a
$\text{CH}_2\text{NHCN} \rightarrow \text{CH}_2 + \text{HNCN}$	1.00E-09	0	1.9	a
$\text{CH}_2\text{NHCN} \rightarrow \text{CH}_2\text{NH} + \text{CN}$	1.00E-09	0	1.9	a
$\text{CH}_3\text{NH} \rightarrow \text{CH}_2\text{NH} + \text{H}$	1.00E-09	0	1.9	a
$\text{CH}_3\text{NH} \rightarrow \text{CH}_3 + \text{NH}$	1.00E-09	0	1.9	a
<b>Ion-neutral</b>				
	(-)	( $cm^3 s^{-1}$ )	(-)	
$\text{C}^+ + \text{NH}_2\text{CH}_2\text{CN} \rightarrow \text{C}_2\text{H}_4\text{N}_2^+ + \text{C}$	0.25	1.75E-09	4.09	b
$\text{C}^+ + \text{NH}_2\text{CH}_2\text{CN} \rightarrow \text{C}_2\text{N}^+ + \text{CH}_2\text{NH}_2$	0.25	1.75E-09	4.09	b
$\text{C}^+ + \text{NH}_2\text{CH}_2\text{CN} \rightarrow \text{H}_2\text{NC}^+ + \text{H}_2\text{CCN}$	0.25	1.75E-09	4.09	b
$\text{C}^+ + \text{NH}_2\text{CH}_2\text{CN} \rightarrow \text{HC}_3\text{NH}^+ + \text{NH}_2$	0.25	1.75E-09	4.09	b
$\text{H}^+ + \text{NH}_2\text{CH}_2\text{CN} \rightarrow \text{C}_2\text{H}_4\text{N}_2^+ + \text{H}$	0.20	5.54E-09	4.09	b
$\text{H}^+ + \text{NH}_2\text{CH}_2\text{CN} \rightarrow \text{HCN}^+ + \text{CH}_2\text{NH}_2$	0.20	5.54E-09	4.09	b
$\text{H}^+ + \text{NH}_2\text{CH}_2\text{CN} \rightarrow \text{CH}_3\text{NH}_2^+ + \text{CN}$	0.20	5.54E-09	4.09	b
$\text{H}^+ + \text{NH}_2\text{CH}_2\text{CN} \rightarrow \text{NH}_3^+ + \text{H}_2\text{CCN}$	0.20	5.54E-09	4.09	b
$\text{H}^+ + \text{NH}_2\text{CH}_2\text{CN} \rightarrow \text{CH}_3\text{CN}^+ + \text{NH}_2$	0.20	5.54E-09	4.09	b
$\text{He}^+ + \text{NH}_2\text{CH}_2\text{CN} \rightarrow \text{CH}_2\text{NH}_2^+ + \text{CN} + \text{He}$	0.25	2.84E-09	4.09	b
$\text{He}^+ + \text{NH}_2\text{CH}_2\text{CN} \rightarrow \text{CH}_2\text{NH}_2 + \text{CN}^+ + \text{He}$	0.25	2.84E-09	4.09	b
$\text{He}^+ + \text{NH}_2\text{CH}_2\text{CN} \rightarrow \text{CH}_2\text{CN}^+ + \text{NH}_2 + \text{He}$	0.25	2.84E-09	4.09	b
$\text{He}^+ + \text{NH}_2\text{CH}_2\text{CN} \rightarrow \text{H}_2\text{CCN} + \text{NH}_2^+ + \text{He}$	0.25	2.84E-09	4.09	b



Continuation of Table 1

Reaction	$\alpha$	$\beta$	$\gamma$	Ref.
CN + CH <sub>3</sub> NH <sub>2</sub> → CH <sub>3</sub> NH + HCN	3.94E-10	0.0	0.00E+00	c
CN + CH <sub>3</sub> NH <sub>2</sub> → CH <sub>2</sub> NH <sub>2</sub> + HCN	8.87E-10	0.0	0.00E+00	c
CN + CH <sub>3</sub> NH <sub>2</sub> → NH <sub>2</sub> CH <sub>2</sub> CN + H	1.73E-17	0.0	0.00E+00	c
HNC + CH <sub>3</sub> NH → CH <sub>3</sub> NHCN + H	8.70E-17	0.5	3.49E+03	d
OH + NH <sub>2</sub> CH <sub>2</sub> CN → NHCH <sub>2</sub> CN + H <sub>2</sub> O	4.31E-10	0.5	1.11E+03	d
NH <sub>2</sub> + NH <sub>2</sub> CH <sub>2</sub> CN → NHCH <sub>2</sub> CN + NH <sub>3</sub>	4.69E-10	0.5	3.77E+03	d
CH <sub>2</sub> OH + NH <sub>2</sub> CH <sub>2</sub> CN → NHCH <sub>2</sub> CN + CH <sub>3</sub> OH	4.48E-10	0.5	5.10E+03	d
CH <sub>3</sub> O + NH <sub>2</sub> CH <sub>2</sub> CN → NHCH <sub>2</sub> CN + CH <sub>3</sub> OH	4.28E-10	0.5	3.05E+03	d
OH + CH <sub>3</sub> NHCN → CH <sub>2</sub> NHCN + H <sub>2</sub> O	5.05E-10	0.5	4.30E+02	d
NH <sub>2</sub> + CH <sub>3</sub> NHCN → CH <sub>2</sub> NHCN + NH <sub>3</sub>	5.48E-10	0.5	4.01E+03	d
CH <sub>2</sub> OH + CH <sub>3</sub> NHCN → CH <sub>2</sub> NHCN + CH <sub>3</sub> OH	5.16E-10	0.5	4.47E+03	d
CH <sub>3</sub> O + CH <sub>3</sub> NHCN → CH <sub>2</sub> NHCN + CH <sub>3</sub> OH	4.94E-10	0.5	2.78E+03	d
OH + CH <sub>3</sub> NCNH → CH <sub>2</sub> NCNH + H <sub>2</sub> O	5.28E-10	0.5	7.07E+02	d
NH <sub>2</sub> + CH <sub>3</sub> NCNH → CH <sub>2</sub> NCNH + NH <sub>3</sub>	5.72E-10	0.5	4.42E+03	d
CH <sub>2</sub> OH + CH <sub>3</sub> NCNH → CH <sub>2</sub> NCNH + CH <sub>3</sub> OH	5.37E-10	0.5	4.47E+03	d
CH <sub>3</sub> O + CH <sub>3</sub> NCNH → CH <sub>2</sub> NCNH + CH <sub>3</sub> OH	5.15E-10	0.5	2.99E+03	d
OH + CH <sub>3</sub> NCNH → CH <sub>3</sub> NCN + H <sub>2</sub> O	5.28E-10	0.5	0.00E+00	d
NH <sub>2</sub> + CH <sub>3</sub> NCNH → CH <sub>3</sub> NCN + NH <sub>3</sub>	5.72E-10	0.5	1.74E+03	d
CH <sub>2</sub> OH + CH <sub>3</sub> NCNH → CH <sub>3</sub> NCN + CH <sub>3</sub> OH	5.37E-10	0.5	2.49E+03	d
CH <sub>3</sub> O + CH <sub>3</sub> NCNH → CH <sub>3</sub> NCN + CH <sub>3</sub> OH	5.15E-10	0.5	9.55E+02	d
Dissociative Recombination	( <i>cm</i> <sup>3</sup> <i>s</i> <sup>-1</sup> )	(-)	(-)	
C <sub>2</sub> H <sub>4</sub> N <sub>2</sub> <sup>+</sup> + e <sup>-</sup> → CH <sub>2</sub> NH <sub>2</sub> + CN	1.50E-07	-0.5	0	a
C <sub>2</sub> H <sub>4</sub> N <sub>2</sub> <sup>+</sup> + e <sup>-</sup> → H <sub>2</sub> CCN + NH <sub>2</sub>	1.50E-07	-0.5	0	a
C <sub>2</sub> H <sub>4</sub> N <sub>2</sub> <sup>+</sup> + e <sup>-</sup> → CH <sub>3</sub> NH + CN	1.50E-07	-0.5	0	a
C <sub>2</sub> H <sub>4</sub> N <sub>2</sub> <sup>+</sup> + e <sup>-</sup> → CH <sub>3</sub> + HNCN	1.50E-07	-0.5	0	a
C <sub>2</sub> H <sub>5</sub> N <sub>2</sub> <sup>+</sup> + e <sup>-</sup> → NH <sub>2</sub> CH <sub>2</sub> CN + H	1.50E-07	-0.5	0	a
C <sub>2</sub> H <sub>5</sub> N <sub>2</sub> <sup>+</sup> + e <sup>-</sup> → CH <sub>2</sub> NH <sub>2</sub> + HNC	1.50E-07	-0.5	0	a
C <sub>2</sub> H <sub>5</sub> N <sub>2</sub> <sup>+</sup> + e <sup>-</sup> → CH <sub>3</sub> CN + NH <sub>2</sub>	1.50E-07	-0.5	0	a
C <sub>2</sub> H <sub>5</sub> N <sub>2</sub> <sup>+</sup> + e <sup>-</sup> → CH <sub>3</sub> NHCN + H	1.50E-07	-0.5	0	a
C <sub>2</sub> H <sub>5</sub> N <sub>2</sub> <sup>+</sup> + e <sup>-</sup> → CH <sub>3</sub> NCNH + H	1.50E-07	-0.5	0	a
C <sub>2</sub> H <sub>5</sub> N <sub>2</sub> <sup>+</sup> + e <sup>-</sup> → CH <sub>3</sub> NH <sub>2</sub> + CN	1.50E-07	-0.5	0	a
C <sub>2</sub> H <sub>5</sub> N <sub>2</sub> <sup>+</sup> + e <sup>-</sup> → CH <sub>3</sub> + NH <sub>2</sub> CN	1.50E-07	-0.5	0	a
CH <sub>3</sub> NH <sup>+</sup> + e <sup>-</sup> → CH <sub>3</sub> + NH	1.50E-07	-0.5	0	a

<sup>a</sup> Estimation according to analogous reaction rate coefficients in the OSU and KIDA network (Hasegawa et al. (1992); Garrod et al. (2007); Hassel et al. (2008); Quan et al. (2010); Wakelam et al. (2015)).

<sup>b</sup> Rate coefficients for unmeasured reactions between ions and neutral species with a dipole moment are computed using the Su-Chesnavich capture approach. This approach is discussed in Su & Chesnavich (1982); Woon & Herbst (2009).

<sup>c</sup> Puzzarini et al. (2020).

<sup>d</sup> This work, based on potential and barrier calculations.

### 3 ASTROCHEMICAL MODEL

To investigate the formation and destruction mechanism of AAN and its isomers MCA, MCI, we use the three-phase NAUTILUS chemical code (Ruaud et al. 2016), which includes the gas, the dust grain surface and the icy mantle. In this study, our gas phase chemistry is based on the public chemical network kida.uva.2014 (Wakelam et al. 2015). The network for surface reactions and gas-grain interactions is based on the one from Garrod et al. (2007) with several additional processes from (Ruaud et al. 2015). And the chemical network has been updated by incorporating the chemistry of HNCO and its metastable isomers, ethanimine ( $\text{CH}_3\text{CHNH}$ ), cyanomethanimine (E-, Z-HNCHCN,  $\text{CH}_2\text{NCN}$ ) and cyanamide ( $\text{NH}_2\text{CN}$ ) (Quan et al. 2010, 2016; Zhang et al. 2020, 2023). Additionally, reactions related to propylene oxide have been integrated based on the work of Das et al. (2019). Given the significance of radical-radical chemical reactions in the formation of Complex Organic Molecules (COMs), particularly in ice chemistry, we have also included the chemical network proposed by Belloche et al. (2014) and Garrod et al. (2017). We added more than 300 reactions concerning AAN, MCA and MCI into our initial gas-grain chemical network, as listed in Table 1 and Table 2. Table 3 shows a selection of species' binding energies used in our model. The rate constants of reactions are calculated by the corresponding equations according to Hasegawa et al. (1992), and Ruaud et al. (2016) on surface and mantle phases. Since Graedel et al. (1982) proposed that the physical assumptions of the process, where diffuse interstellar material collapses into denser clouds, are more suitable for the low metal abundance model, based on a comparison of observations of several molecules and model results, we used the standard oxygen-rich low-metal initial elemental abundances from Graedel et al. (1982), as well as Quan & Herbst (2007), as listed in Table 4. All abundances are given with respect to the total hydrogen density. The code simulates chemistry in three phases i.e., gas-phase, grain surface, and icy mantle, and also considers various possible exchanges among the different phases via accretion of gas phase species onto grain surfaces, thermal and non-thermal desorption of species from grain surface into the gas phase. The latter includes cosmic-ray desorption, photodesorption via external photons or those via photons produced by cosmic rays (Öberg et al. 2007), and reactive desorption using the Rice-Ramsperger-Kassel (RRK) approach (Garrod et al. 2007). The surface-mantle and mantle-surface exchange of species is also considered. The diffusion energy to binding energy ratio assumes to be 0.5 for all species on the surface and in ice mantle, respectively. Grains are assumed to be spherical with the radii of  $0.1 \mu\text{m}$ . The grain density is  $3 \text{ g cm}^{-3}$  and the gas-to-dust mass ratio is 100.

AAN has only been detected in the high mass star formation region Sgr B2(N). MCA and MCI have not yet been detected in any sources so far. Therefore, we simulated the physical conditions where AAN was detected, i.e., the hot cores. Correspondingly, we applied hot core models to simulate the formation and destruction processes of AAN, MCA and MCI. Star formation can be divided into two stages based on different periods of evolution. The first stage involves the simulation of protostar growth through the accretion of the outer envelope region, known as the free-fall collapse process or prestellar phase. During this stage, which lasts approximately  $1 \times 10^6$  yr, the temperature remains consistently low, while the density gradually increases over time, resulting in an increase in extinction. The initial gas and grain temperatures are set at 10 K, the initial gas density is  $3 \times 10^3 \text{ cm}^{-3}$ , and the final collapse density is  $1.6 \times 10^7 \text{ cm}^{-3}$ . The second stage is the warm-up stage, where the temperature increases according to the formula  $T = T_0 + (T_{\text{max}} - T_0)(\Delta t/t_h)^n$  (Garrod &

Herbst 2006), with  $n = 2$ ,  $t_h = 2 \times 10^5$  yr,  $\Delta t = (t - t_0)$ , and  $t_0 = 1 \times 10^5$  yr. After an initial cold phase of  $1 \times 10^5$  yr, the gas and grain temperatures increase from 10 K to the maximum values of  $T_{\text{max}}$ , reaching 150 K and 200 K within a time frame of  $2 \times 10^5$  yr. Once the maximum value is reached, the temperature remains constant. During this stage, it is assumed that the gas and dust temperatures are well coupled. The major physical parameters of hot core models are summarized in Table 5.

## 4 RESULTS

### 4.1 Hot cores

The results of fractional abundances of AAN, MCA, and MCI molecules with respect to total hydrogen ( $n_H$ ) for two warm-up models are presented in Fig. 3. These models correspond to different maximum temperatures ( $T_{\text{max}} = 150, 200$  K). The physical parameters used in the models are based on the sources of Sgr B2(N) suggested by Bonfand et al. (2019). In Fig. 3, the gray and light gray rectangles represent the observed abundances of AAN in Sgr B2(N1) and Sgr B2(N2), respectively, with an uncertainty of  $\pm$  a factor of 3. The observational results for AAN in Sgr B2(N1) and Sgr B2(N2) were obtained from Melosso et al. (2020) and Richard et al. (2018), respectively. For the hot cores Sgr B2(N1) and Sgr B2(N2), we adopted the hydrogen column density of  $1.54 \times 10^{25} \text{ cm}^{-2}$  and  $1.42 \times 10^{24} \text{ cm}^{-2}$  respectively, as reported by Bonfand et al. (2017, 2019). The observed abundances of AAN were  $\sim 7.14 \times 10^{-9}$  and  $\sim 6.83 \times 10^{-8}$  in Sgr B2(N1) and Sgr B2(N2), respectively. Here we compare the simulated results with observations toward Sgr B2(N) in Fig. 3.

The warm-up models produce sufficient abundances of AAN during the warm-up process, reaching maximum temperatures of 150 and 200 K at a hydrogen density of  $1.6 \times 10^7 \text{ cm}^{-3}$ . At these temperatures, the peak gas phase fractional abundances of AAN can reach  $2.23 \times 10^{-8}$  and  $1.93 \times 10^{-8}$  at the time of  $2.89 \times 10^5$  yr and  $2.64 \times 10^5$  yr, respectively. Our simulated results are found to be in good agreement with the observed values of Sgr B2(N1) within the time range of  $(2.74 - 5.63) \times 10^5$  yr and  $(2.51 - 4.53) \times 10^5$  yr at  $T_{\text{max}}$  of 150 K and 200 K, respectively. For Sgr B2(N2), the model results are unable to match the observed abundance at these maximum temperatures. In our models, the peak gas phase fractional abundances of MCA can reach  $1.77 \times 10^{-10}$  and  $1.39 \times 10^{-10}$  at the time of  $3.92 \times 10^5$  yr and  $3.40 \times 10^5$  yr for  $T_{\text{max}} = 150$  K and 200 K, respectively. For MCI, the peak values are  $4.88 \times 10^{-11}$  and  $7.74 \times 10^{-11}$  at the time of  $4.22 \times 10^5$  yr and  $3.65 \times 10^5$  yr for  $T_{\text{max}} = 150$  K and 200 K, respectively.

Gas phase AAN mainly originate from the surface through thermal desorption processes. A significant amount of surface AAN desorb into the gas phase at temperature up to approximately 100 K, which is lower than the experimental results  $\geq 190$  K from Borget et al. (2012). We utilized a binding energy of 5480 K for all three isomers (Garrod 2013), as presented in Table 3. As illustrated in Fig. 3, it can be seen that the abundances of the three isomers increase significantly as the temperature rises. This can be attributed to the availability of sufficient thermal energy to enable reactants to overcome the diffusion barriers and react with each other on the grain surface, leading to the formation of products that evaporated into gas phase at a temperature of approximately 100 K.

During the warm-up stage, there are several major formation reactions involved in the production of AAN on the grain surface, including  $\text{NH}_2 + \text{H}_2\text{CCN}$ ,  $\text{HNC} + \text{CH}_2\text{NH}$  and  $\text{NHCH}_2\text{CN} + \text{H}$ .

**Table 2.** Activation energy barrier values of important surface/mantle reactions.

Surface reactions	$E_a$ (K)	Ref.
$\text{CN} + \text{CH}_2\text{NH}_2 \rightarrow \text{NH}_2\text{CH}_2\text{CN}$	0	a
$\text{NH}_2 + \text{H}_2\text{CCN} \rightarrow \text{NH}_2\text{CH}_2\text{CN}$	0	a
$\text{HCN} + \text{CH}_2\text{NH} \rightarrow \text{NH}_2\text{CH}_2\text{CN}$	3.17E+03	b
$\text{HNC} + \text{CH}_2\text{NH} \rightarrow \text{NH}_2\text{CH}_2\text{CN}$	3.52E+02	b
$\text{NH} + \text{H}_2\text{CCN} \rightarrow \text{NHCH}_2\text{CN}$	0	a
$\text{CN} + \text{CH}_2\text{NH} \rightarrow \text{NHCH}_2\text{CN}$	0	c
$\text{NH}_2 + \text{HCCN} \rightarrow \text{NH}_2\text{CHCN}$	0	d
$\text{E-HNCHCN} + \text{H} \rightarrow \text{NH}_2\text{CHCN}$	1.40E+03	e
$\text{Z-HNCHCN} + \text{H} \rightarrow \text{NH}_2\text{CHCN}$	1.30E+03	e
$\text{NHCH}_2\text{CN} + \text{H} \rightarrow \text{NH}_2\text{CH}_2\text{CN}$	0	a
$\text{NH}_2\text{CHCN} + \text{H} \rightarrow \text{NH}_2\text{CH}_2\text{CN}$	0	d
$\text{H} + \text{CH}_2\text{NH} \rightarrow \text{CH}_3\text{NH}$	0	f
$\text{NH} + \text{CH}_3 \rightarrow \text{CH}_3\text{NH}$	0	d
$\text{H} + \text{CH}_3\text{NH} \rightarrow \text{CH}_3\text{NH}_2$	0	f
$\text{CH}_3 + \text{HNCN} \rightarrow \text{CH}_3\text{NHCN}$	0	d
$\text{CH}_3 + \text{HNCN} \rightarrow \text{CH}_3\text{NCNH}$	0	d
$\text{CN} + \text{CH}_3\text{NH} \rightarrow \text{CH}_3\text{NHCN}$	0	d
$\text{HNC} + \text{CH}_3\text{NH} \rightarrow \text{CH}_3\text{NHCN} + \text{H}$	3.49E+03	d
$\text{H} + \text{CH}_2\text{NCN} \rightarrow \text{CH}_3\text{NCN}$	1.19E+03	d
$\text{H} + \text{CH}_2\text{NCN} \rightarrow \text{CH}_2\text{NCNH}$	3.71E+03	d
$\text{H} + \text{CH}_3\text{NCN} \rightarrow \text{CH}_3\text{NHCN}$	0	d
$\text{H} + \text{CH}_3\text{NCN} \rightarrow \text{CH}_3\text{NCNH}$	0	d
$\text{H} + \text{CH}_2\text{NCNH} \rightarrow \text{CH}_3\text{NCNH}$	0	d
$\text{OH} + \text{NH}_2\text{CH}_2\text{CN} \rightarrow \text{H}_2\text{O} + \text{NHCH}_2\text{CN}$	1.11E+03	g, d
$\text{NH}_2 + \text{NH}_2\text{CH}_2\text{CN} \rightarrow \text{NH}_3 + \text{NHCH}_2\text{CN}$	3.77E+03	g, d
$\text{CH}_2\text{OH} + \text{NH}_2\text{CH}_2\text{CN} \rightarrow \text{CH}_3\text{OH} + \text{NHCH}_2\text{CN}$	5.10E+03	g, d
$\text{CH}_3\text{O} + \text{NH}_2\text{CH}_2\text{CN} \rightarrow \text{CH}_3\text{OH} + \text{NHCH}_2\text{CN}$	3.05E+03	g, d
$\text{OH} + \text{CH}_3\text{NHCN} \rightarrow \text{CH}_2\text{NHCN} + \text{H}_2\text{O}$	4.30E+02	d
$\text{NH}_2 + \text{CH}_3\text{NHCN} \rightarrow \text{CH}_2\text{NHCN} + \text{NH}_3$	4.01E+03	d
$\text{CH}_2\text{OH} + \text{CH}_3\text{NHCN} \rightarrow \text{CH}_2\text{NHCN} + \text{CH}_3\text{OH}$	4.47E+03	d
$\text{CH}_3\text{O} + \text{CH}_3\text{NHCN} \rightarrow \text{CH}_2\text{NHCN} + \text{CH}_3\text{OH}$	2.78E+03	d
$\text{OH} + \text{CH}_3\text{NCNH} \rightarrow \text{CH}_2\text{NCNH} + \text{H}_2\text{O}$	7.07E+02	d
$\text{NH}_2 + \text{CH}_3\text{NCNH} \rightarrow \text{CH}_2\text{NCNH} + \text{NH}_3$	4.42E+03	d
$\text{CH}_2\text{OH} + \text{CH}_3\text{NCNH} \rightarrow \text{CH}_2\text{NCNH} + \text{CH}_3\text{OH}$	4.47E+03	d
$\text{CH}_3\text{O} + \text{CH}_3\text{NCNH} \rightarrow \text{CH}_2\text{NCNH} + \text{CH}_3\text{OH}$	2.99E+03	d
$\text{OH} + \text{CH}_3\text{NCNH} \rightarrow \text{CH}_3\text{NCN} + \text{H}_2\text{O}$	0.00E+00	d
$\text{NH}_2 + \text{CH}_3\text{NCNH} \rightarrow \text{CH}_3\text{NCN} + \text{NH}_3$	1.74E+03	d
$\text{CH}_2\text{OH} + \text{CH}_3\text{NCNH} \rightarrow \text{CH}_3\text{NCN} + \text{CH}_3\text{OH}$	2.49E+03	d
$\text{CH}_3\text{O} + \text{CH}_3\text{NCNH} \rightarrow \text{CH}_3\text{NCN} + \text{CH}_3\text{OH}$	9.55E+02	d

The dust surface reactions related to AAN, MCA and MCI are shown.  $E_a$  represents the value of the activation barrier. Since radical species are so reactive, radical–radical reactions would have no activation barriers.

<sup>a</sup> Belloche et al. (2009). <sup>b</sup> Xu & Wang (2007); Koch et al. (2008). <sup>c</sup> Basiuk (2001).

<sup>d</sup> This work, based on potential and barrier calculations.

<sup>e</sup> Shingledecker et al. (2020). <sup>f</sup> Woon (2002); Suzuki et al. (2016). <sup>g</sup> Garrod (2013).

**Table 3.** Binding energies of involved species.

Species	$E_{\text{des}}$ (K)	Ref.
$\text{NH}_2\text{CH}_2\text{CN}$	5480	Garrod (2013)
$\text{NHCH}_2\text{CN}$	5030	$\text{NH}_2\text{CH}_2\text{CN-H}$
$\text{NH}_2\text{CHCN}$	5030	$\text{NH}_2\text{CH}_2\text{CN-H}$
$\text{CH}_3\text{NH}$	3414	Das et al. (2018)
$\text{CH}_3\text{NHCN}$	5480	$\text{NH}_2\text{CH}_2\text{CN}$
$\text{CH}_3\text{NCNH}$	5480	$\text{NH}_2\text{CH}_2\text{CN}$
$\text{CH}_3\text{NCN}$	5030	$\text{NHCH}_2\text{CN}$
$\text{CH}_2\text{NCNH}$	5030	$\text{NHCH}_2\text{CN}$
$\text{CH}_2\text{NHCN}$	5030	$\text{NHCH}_2\text{CN}$

$\text{NHCH}_2\text{CN}$  is formed through the reactions of  $\text{NH} + \text{H}_2\text{CCN}$  and  $\text{CN} + \text{CH}_2\text{NH}$  on the grain surface. The first formation route agrees

with the modeling result of Garrod (2013), while the validity of the third route has been supported by Belloche et al. (2009). Although, the gaseous AAN primarily originates from the thermal desorption process of grain surface, the peak abundance of AAN in the gas phase exceeds its peak abundances on grain surface in our models. This can be explained as follows: When AAN reaches its peak abundance in the gas phase, the reaction of  $\text{CH}_2\text{NH} + \text{HNC}$  on grain surface is the major formation route for AAN. Simultaneously,  $\text{CH}_2\text{NH}$  is formed through two pathways: the thermal desorption process and the reaction of  $\text{NH} + \text{CH}_3$  in the gas phase. This results in a significant increase in the abundance of  $\text{CH}_2\text{NH}$  in the gas phase. Additionally, more  $\text{CH}_2\text{NH}$  accretes on the grain surface according to the equation for the rate of accretion of a gas-phase species (Semenov et al. 2010). Subsequently, more gaseous AAN is produced as  $\text{CH}_2\text{NH}$  reacts with HNC to form AAN on the grain surface, followed by the thermal desorption process. As a result, the gas phase abundances

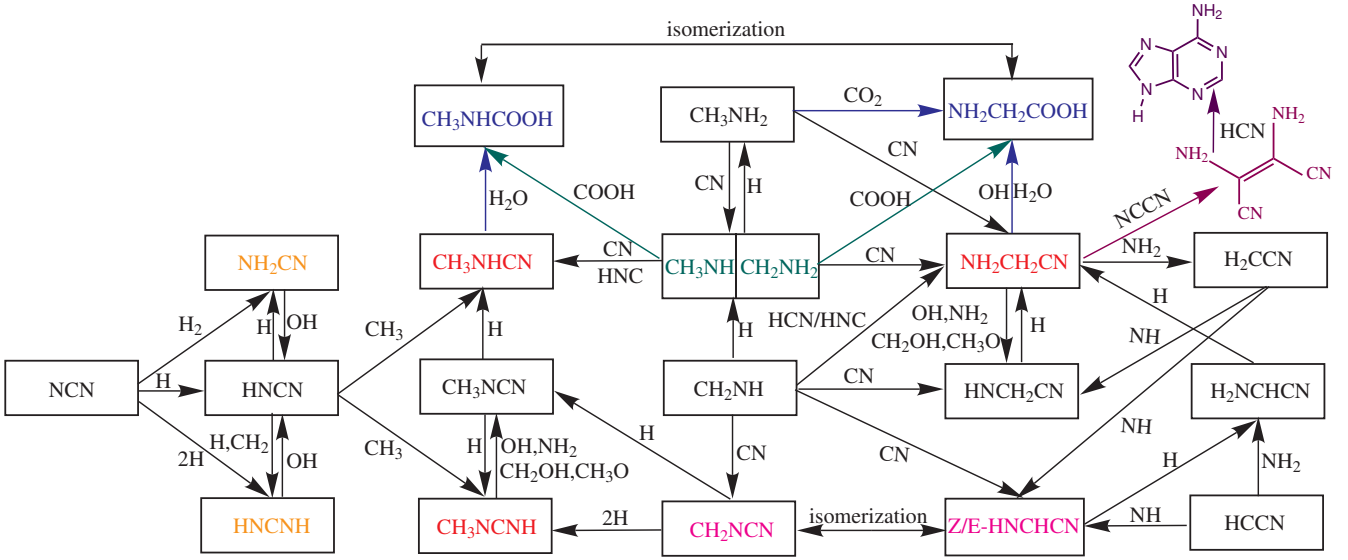


**Figure 2.** The neutral-neutral reactions linking the AAN and its isomers, with species of the same color indicating isomers. Blue arrows are for hydrolysis reactions. Green arrows denote the reactions for the formation of glycine and its isomer on the grain surfaces. Purple and dark purple arrows and corresponding species represent these reactions need to be clarified by theoretical and experimental studies. All these reactions are currently not included in our network.

**Table 4.** Initial elemental abundance compared to total proton density of chemical models.

Species	Abundance
He	$6.00 \times 10^{-2}$
N	$2.14 \times 10^{-5}$
O	$1.76 \times 10^{-4}$
H <sub>2</sub>	$5.00 \times 10^{-1}$
C <sup>+</sup>	$7.30 \times 10^{-5}$
S <sup>+</sup>	$8.00 \times 10^{-8}$
Si <sup>+</sup>	$8.00 \times 10^{-9}$
Fe <sup>+</sup>	$3.00 \times 10^{-9}$
Na <sup>+</sup>	$2.00 \times 10^{-9}$
Mg <sup>+</sup>	$9.00 \times 10^{-9}$
P <sup>+</sup>	$3.00 \times 10^{-9}$
Cl <sup>+</sup>	$4.00 \times 10^{-9}$
F <sup>+</sup>	$6.69 \times 10^{-9}$

of AAN exceed its grain surface phase abundances. On the other hand, MCA and MCI are primarily formed through the reactions of  $\text{CH}_3\text{NCN} + \text{H}$  on the grain surface and the electronic recombination of ion  $\text{C}_2\text{H}_5\text{N}_2^+$  in the gas phase.  $\text{CH}_3\text{NCN}$  is produced through the hydrogenation reaction of  $\text{CH}_2\text{NCN}$  on the grain surface. In our previous modeling work, we found that  $\text{CH}_2\text{NCN}$  is present in relatively low abundance (Zhang et al. 2020). Recently, it has been detected in the Galactic Center G+0.693-0.027 molecular cloud (San Andrés et al. 2024). The  $\text{C}_2\text{H}_5\text{N}_2^+$  ion is mainly formed via the ion-neutral reaction of AAN. Eventually, as the temperature reaches 100 K, the isomers efficiently desorb from the grain surface into the gas phase. This desorption behavior during the warm-up stage aligns with the mechanism proposed by Garrod & Herbst (2006) for studying complex organic molecules in ISM. However, after reaching their peak abundances, the three isomers abundances subsequently decline due to active destruction reactions in the gas phase, including reactions with positive ions such as  $\text{H}^+$ ,  $\text{H}_3^+$ ,  $\text{C}^+$ ,  $\text{He}^+$  and  $\text{H}_3\text{O}^+$ , as well as the free radical OH. As illustrated in Fig. 3, there are rapidly decreasing abundance for these isomers at  $T_{\text{max}} = 200$  K due to the higher

temperature results in a higher destruction rate comparing to  $T_{\text{max}} = 150$  K.

In our models, the difference in abundances between AAN and MCA, as well as between MCA and MCI, is around 1 to 2 orders of magnitude at  $T_{\text{max}} = 150$  K. However, at  $T_{\text{max}} = 200$  K, the difference between MCA and MCI is less than one order of magnitude. Thus, the discrepancy in the abundances of three isomers is significant at different maximum temperatures. We speculated that MCA and MCI could be potential interstellar molecules and may be detectable in the sources where AAN is abundant, using available spectral data. Since a large part of MCA and MCI are derived from the ion-neutral reactions of AAN and subsequently by the electronic recombination of ion  $\text{C}_2\text{H}_5\text{N}_2^+$  in the gas phase. However, due to its higher structural instability and rapid chemical destructive rate, MCI is more challenging to detect in the ISM compared to MCA.

In high mass star formation regions, there is a significant presence of UV radiation. Therefore, in order to further simulate the physical conditions in Sgr B2(N), we utilized two higher values of UV factor, 10 and 100 times larger than the normal value for models with a hydrogen density of  $1.6 \times 10^7 \text{ cm}^{-3}$ . It should be noted that only the warm-up stage in the models adopted the high UV factors. The results of these simulations are shown in Fig. 4. It can be seen that fractional abundances of AAN are lower comparing to the results obtained from the standard UV factor computations, for both  $T_{\text{max}}$  of 150 and 200 K. The stronger UV radiations lead to high photodissociation rate for the three isomers. The peak abundance of AAN drops from  $2.23 \times 10^{-8}$  to  $2.03 \times 10^{-8}$  at a time of  $2.89 \times 10^5$  yr as the UV factor increases from 1 to 10 for  $T_{\text{max}}$  of 150 K. For the case of UV factor of 100, it has the same trend as the UV factor of 10, and the peak abundance of AAN deduced to  $1.98 \times 10^{-8}$  at the same time. For  $T_{\text{max}} = 200$  K, the abundance of AAN decreases from  $1.93 \times 10^{-8}$  to  $1.73 \times 10^{-8}$  at a time of  $2.64 \times 10^5$  yr as the UV factor increases from 1 to 10. When a UV factor of 100 is applied, the abundance of AAN further reduced to  $1.55 \times 10^{-8}$ . A higher temperature leads to a lower abundance of AAN compared to  $T_{\text{max}} = 150$  K, as the higher temperature results in a higher destruction rate. However, the high UV factor only slightly reduces the abundance of AAN compared

**Table 5.** Physical parameters of hot core models

Source (Stage)	$n_{\text{H}}$ ( $\text{cm}^{-3}$ )	T (K)	$A_V$ (mag)	$\zeta$ ( $\text{s}^{-1}$ )	UV factor (Habing)
The freefall collapse <sup>a,b</sup>	$3 \times 10^3 \rightarrow 1.6 \times 10^7$	10	$2 \rightarrow 6.109 \times 10^2$	$1.3 \times 10^{-17}$	1
The warm-up <sup>b,c</sup>	$1.6 \times 10^7$	10 $\rightarrow$ 150, 200	$6.109 \times 10^2$	$1.3 \times 10^{-17}$	1, 10, 100

Notes. <sup>a</sup>Garrod & Herbst (2006), <sup>b</sup>Bonfand et al. (2019), <sup>c</sup>Coutens et al. (2018)

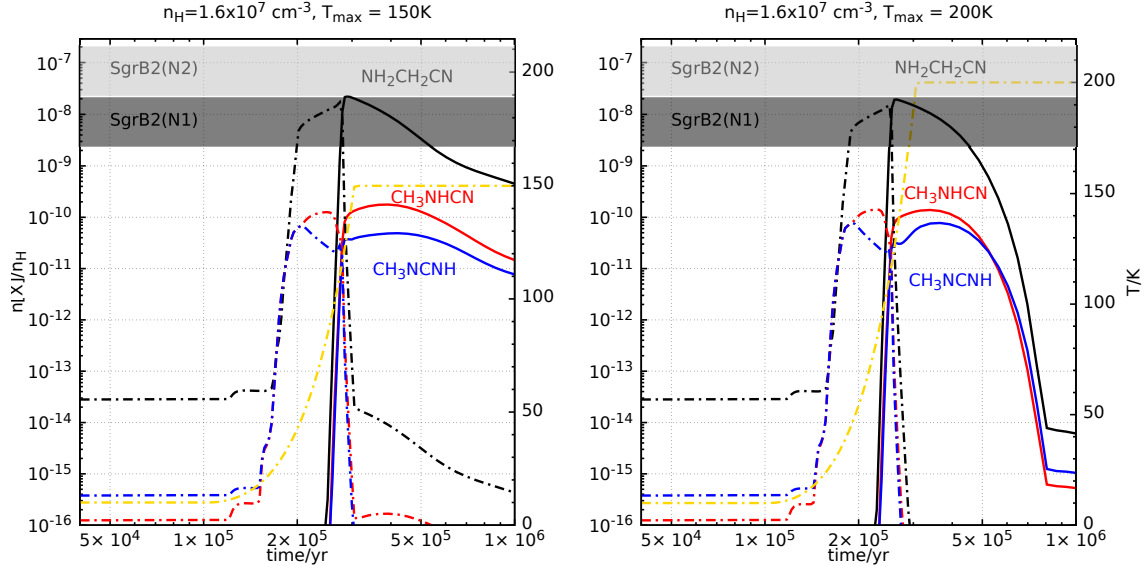


**Figure 3.** The calculated abundances of AAN, MCA and MCI in the gas phase and on grain mantles, including surface and icy mantle, are plotted versus time for warm-up stages in hot core models. The density is  $1.6 \times 10^7 \text{ cm}^{-3}$ , and the temperatures remain at a constant value of 10 K. During the warm-up stage,  $T_{\text{max}}$  adopt two values, 150 and 200 K. Solid lines correspond to the gas phase abundances, dotted lines indicate abundances on the grain mantles. The gray and light gray rectangles represent the observed abundance with  $\pm$  a factor of 3 uncertainty for AAN in Sgr B2(N1) and Sgr B2(N2), respectively. Golden dotted lines denote temperature profiles.

to the simulated result using the standard UV factor. There are also experimental findings that suggest species containing nitriles survive longer than the corresponding amino acids glycine when exposed to UV photolysis in the solid state at 15 K (Bernstein et al. 2004). The simulated abundances of AAN also agree well with the observations within a certain time range, but the time range is shorter than using the standard UV factor, as shown in Fig. 4. Similarly, MCA exhibits a similar trend at high UV factors to AAN, because it also contain nitrile group. Therefore, higher UV factors have minimal effects on the differences in their abundance magnitudes. In contrast, MCI shows a different behavior from AAN and MCA. Its abundance is greatly influenced by UV radiation due to the absence of nitrile group, making it susceptible to UV photodissociation, as shown in Fig. 5.

#### 4.2 The chemical relations among AAN isomers and other species

AAN is a compound that contains both an amino and a nitrile functional group, making it an amino nitrile. In astrobiology, many bi-functional building blocks can undergo cyclization reactions, allowing rapid advance toward prospective heterocyclic units. AAN can synthesize adenine through two-step chemical reactions (Vasconcelos et al. 2020). The simplest amino nitrile is  $\text{NH}_2\text{CN}$  (Cleaves 2011), which can also form adenine via a series of chemical reactions (Merz et al. 2014).  $\text{NH}_2\text{CN}$  has been detected in many different types of star formation regions, as listed in Zhang et al. (2023). Here we cal-

culated the ratio of  $\text{NH}_2\text{CN}$  to AAN and found the same value of 0.1 when their abundances both reach their peaks at  $T_{\text{max}} = 150 \text{ K}$  and  $200 \text{ K}$  corresponding to the time of  $2.89 \times 10^5 \text{ yr}$  and  $2.64 \times 10^5 \text{ yr}$  as shown in Fig. 6. The column density of  $\text{NH}_2\text{CN}$  was  $5.13 \times 10^{16} \text{ cm}^{-2}$  with the rotational temperature of 150 K towards the Sgr B2(N) (Belloche et al. 2013). The column density of AAN is  $9.7 \times 10^{16} \text{ cm}^{-2}$  in the same region with the same rotational temperature (Richard et al. 2018). The observational ratio is 0.53, which is very close to our simulated ratio.

During warm-up stage, both AAN and  $\text{NH}_2\text{CN}$  undergo similar chemical formation processes. Initially, they are formed via free radicals reactions on the grain surface at a relative low temperature. Subsequently, they desorb from the grain surface and enter the gas phase through thermal desorption when the temperature reaches a high value. Therefore, their were mainly detected in star-formation regions. However,  $\text{NH}_2\text{CN}$  is observed in a wider variety of sources due to its smaller size relative to AAN and its more facile formation in ISM. Generally, the smaller molecules of the same family are more abundant than the larger ones. To the contrary, the abundances of AAN, despite its higher molecular mass, are higher than those of  $\text{NH}_2\text{CN}$ . In our models, we found that  $\text{NH}_2\text{CN}$  has higher desorption energy than that of AAN, which may be a contributing factor to this unexpected outcome. However, this does not alter the results when we exchange the desorption energies of  $\text{NH}_2\text{CN}$  and AAN. Therefore, we speculated that the reactants of AAN are easy to form and have high abundances comparing to those of  $\text{NH}_2\text{CN}$ .

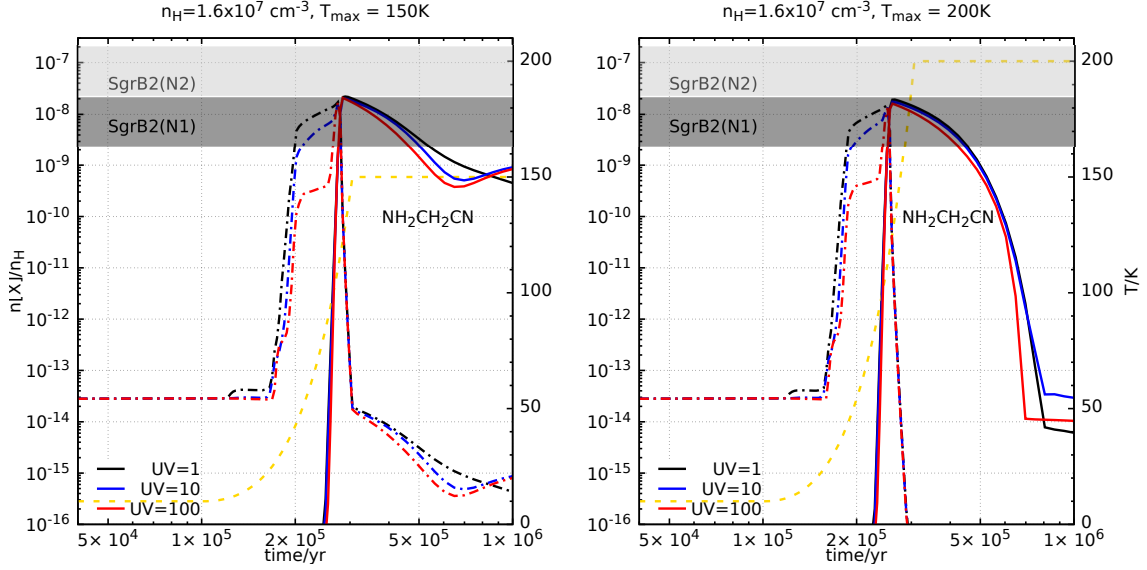
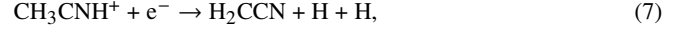


**Figure 4.** The calculated abundances of AAN in the gas phase and on the grain mantle, are plotted versus time for warm-up models with the gas density of  $1.6 \times 10^7 \text{ cm}^{-3}$ . The left panel denotes  $T_{\text{max}}$  of 150 K with different UV factors, and the right panel responds  $T_{\text{max}}$  of 200 K. Solid lines correspond to the gas phase abundances, dotted lines indicate abundances on the grain mantles. The gray and light gray rectangles represent the observed abundance with  $\pm$  a factor of 3 uncertainty for AAN in Sgr B2(N1) and Sgr B2(N2), respectively. Golden dotted lines denote temperature profiles.

APN is another member of the AAN family, which is the next stage in complexity with one additional  $\text{CH}_2$  group. Richard et al. (2018) conducted a search for APN towards the Sgr B2(N), but their attempts were unsuccessful. Based on our present work, we believed that the formation of APN in the ISM is more challenging compared to AAN.

According to Garrod (2013), AAN is primarily formed through the reaction of  $\text{NH}_2 + \text{H}_2\text{CCN}$  on grain surface. However, in our model, this reaction is not the sole major formation pathway. Additionally, their proposal of  $\text{H}_2\text{CCN}$  originating from  $\text{CH}_3\text{CN}$  differs from our results. In our study,  $\text{H}_2\text{CCN}$  is mainly produced via the reaction of  $\text{CN} + \text{CH}_3$  (Reaction (6)), as described by Loison et al. (2014). It could also be formed through the electronic recombination of ion  $\text{CH}_3\text{CNH}^+$  in the gas phase (Reaction (7)). The branching ratio of the channel leading to  $\text{H}_2\text{CCN}$  is approximately 24 percent (Loison et al. 2014). Furthermore,  $\text{CH}_3\text{CNH}^+$  is primarily generated through the reaction of  $\text{HCN} + \text{CH}_3^+$  in the gas phase rather than the protonated  $\text{CH}_3\text{CN}$ . On the other hand,  $\text{CH}_3\text{CN}$  is mainly produced through the electronic recombination of ion  $\text{CH}_3\text{CNH}^+$ , which branching ratio of this channel giving  $\text{CH}_3\text{CN}$  is approximately 39 percent (Reaction (8))(Loison et al. 2014). On grain surface, it is mainly formed by the hydrogenation of  $\text{H}_2\text{CCN}$ . Both  $\text{H}_2\text{CCN}$  and  $\text{CH}_3\text{CN}$  are destroyed by ion-neutral reactions involving  $\text{H}_3^+$  in gas phase, as well as by the hydrogenation reaction on grain surface. Therefore, we concluded that AAN and  $\text{CH}_3\text{CN}$  weakly compete for the utilization of  $\text{H}_2\text{CCN}$  as a precursor on grain surfaces. As shown in Fig. 7, the peak abundance of  $\text{CH}_3\text{CN}$  are  $1.77 \times 10^{-8}$  at  $T_{\text{max}} = 150 \text{ K}$ , which are one order of magnitude higher than the observed towards SgrB2(N) (Belloche et al. 2013). The peak abundance of  $\text{H}_2\text{CCN}$  are  $6.6 \times 10^{-7}$  at  $T_{\text{max}} = 150 \text{ K}$ . However, it has not been detected towards the SgrB2(N) so far. Here we only discussed the results for a temperature of  $T_{\text{max}} = 150 \text{ K}$ , as  $T_{\text{max}} = 200 \text{ K}$  shows a similar trend but with a higher destruction rate.



$\text{CH}_2\text{NH}$  and  $\text{CH}_3\text{NH}$  play a significant role in the formation of AAN and MCA, making them crucial components for the detection of AAN and MCA in the ISM. Additionally,  $\text{CH}_2\text{NH}$  is an important prebiotic molecule that has been suggested as a possible precursor for glycine and its nitrile AAN (Hoyle 1976; Dickerson 1978) and has been detected in several Galactic objects (Godfrey et al. 1973; Dickens et al. 1997; Qin et al. 2010; Halfen et al. 2013; Suzuki et al. 2016). However,  $\text{CH}_3\text{NH}$  has not been detected in any sources thus far. In our models,  $\text{CH}_2\text{NH}$  is formed through both the neutral-neutral reaction of  $\text{NH} + \text{CH}_3$  (Reaction (9)) and the electronic recombination of  $\text{CH}_3\text{NH}_3^+$  ion in gas phase (Reaction (10)), as well as the hydrogenation reaction of  $\text{H} + \text{H}_2\text{CN}$  on the grain surface. It is destroyed through ion-neutral reactions with  $\text{H}_3^+$  in gas phase and through the hydrogenation reaction to form  $\text{CH}_3\text{NH}$  and  $\text{CH}_2\text{NH}_2$  on the grain surface, with activation energies of 2134 K and 3170 K, respectively. This hydrogenation reaction is the major pathway for the formation of  $\text{CH}_3\text{NH}$ .  $\text{CH}_3\text{NH}$  can be formed in gas phase through the reaction of  $\text{CN} + \text{CH}_3\text{NH}_2$ , albeit as a minor contribution.  $\text{CH}_3\text{NH}$  is ultimately transformed into  $\text{CH}_3\text{NH}_2$  on the grain surface, which is also believed to be a potential interstellar precursor to the amino acid glycine, e.g., Bossa et al. (2009); Lee et al. (2009). Halfen et al. (2013) suggested that  $\text{CH}_2\text{NH}$  and  $\text{CH}_3\text{NH}_2$  are formed via different chemical processes in Sgr B2 based on the rotational temperatures and distributions observed in Sgr B2. They also proposed that  $\text{CH}_2\text{NH}$  exists in both a colder, foreground gas and a warmer, background cloud, while  $\text{CH}_3\text{NH}_2$  is present in much warmer gas compared to  $\text{CH}_2\text{NH}$ . This is because  $\text{CH}_3\text{NH}_2$  is primarily formed through the reaction of  $\text{CH}_3\text{NH} + \text{H}$  (major pathway) and  $\text{CH}_2\text{NH}_2 + \text{H}$  (minor pathway) on the grain surface, and when the temperature rises, it evaporates through thermal processes. On the other hand,  $\text{CH}_2\text{NH}$  is formed both in the gas phase through Reaction (9) and to a lesser extent

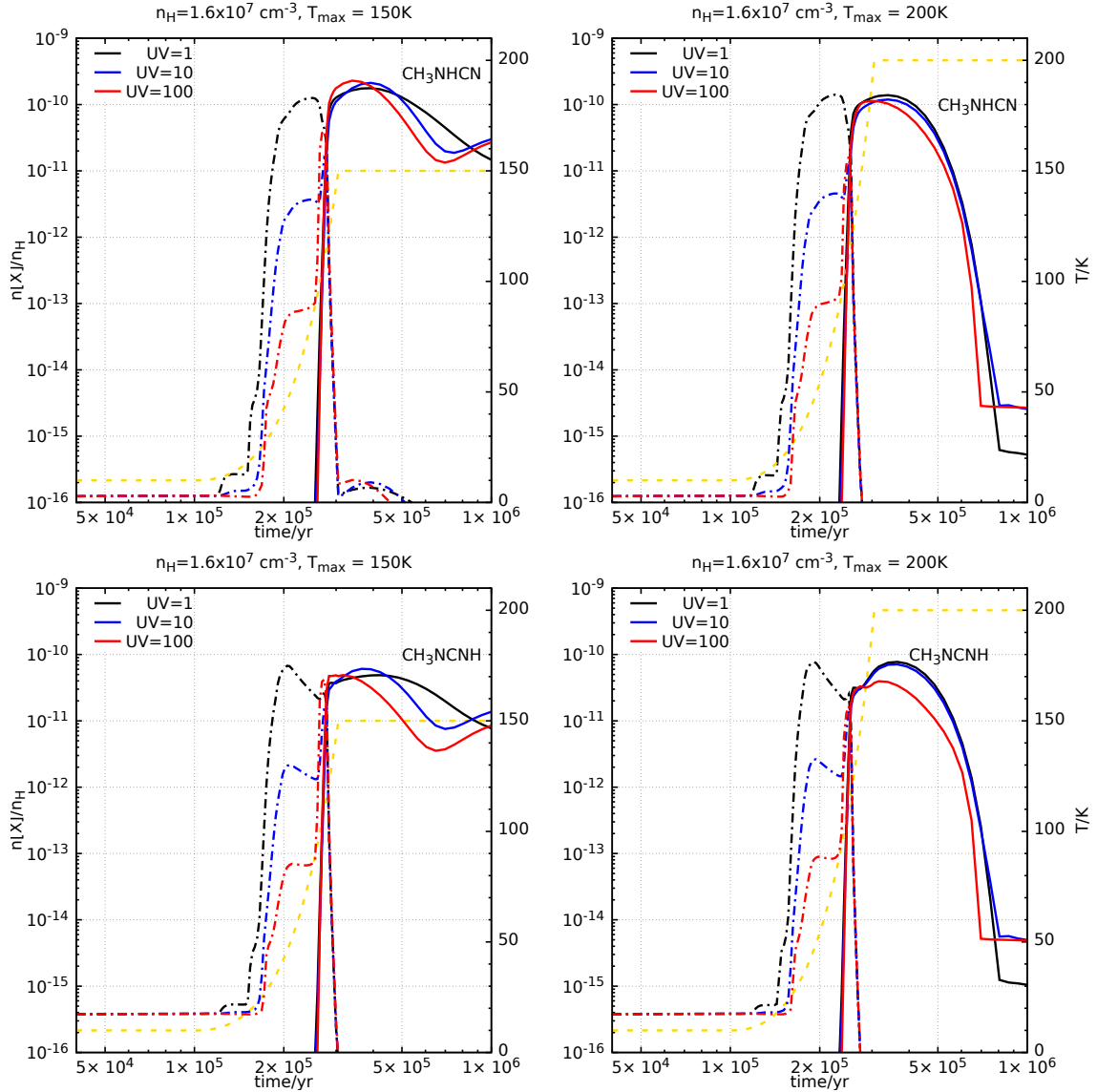
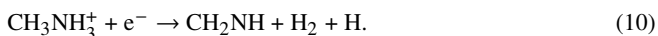


**Figure 5.** The calculated abundances of MCA and MCI in the gas phase and on the grain mantle, are plotted versus time for warm-up models with the gas density of  $1.6 \times 10^7 \text{ cm}^{-3}$ . The left panel denotes  $T_{\text{max}} = 150 \text{ K}$  with different UV factors, and the right panel responds  $T_{\text{max}} = 200 \text{ K}$ . Solid lines correspond to the gas phase abundances, dotted lines indicate abundances on the grain mantles. Golden dotted lines denote temperature profiles.

on grain surface through the reaction of  $\text{H} + \text{H}_2\text{CN}$ . Therefore, it can exist in regions that are not as warm (Halfen et al. 2013). Fig. 7 shows that the peak abundance of  $\text{CH}_2\text{NH}$  is  $8.83 \times 10^{-7}$  at  $T_{\text{max}} = 150 \text{ K}$ , which is one order of magnitude higher than the observation in SgrB2(N) (Belloche et al. 2013; Suzuki et al. 2016), similar to the results of Suzuki et al. (2016). The peak abundance of  $\text{CH}_3\text{NH}_2$  is  $2.93 \times 10^{-7}$  at  $T_{\text{max}} = 150 \text{ K}$ , which is overproduced by one order of magnitude compared to the observation from Belloche et al. (2013). For  $T_{\text{max}} = 200 \text{ K}$ , there is a higher production of  $\text{CH}_2\text{NH}$  molecules compared to  $T_{\text{max}} = 150 \text{ K}$ , but for  $\text{CH}_3\text{NH}_2$ , the trend is similar. Additionally, both exhibit a higher molecular destruction rate.



Cyanogen (NCCN) is another important molecules that may pos-

sible react with AAN to form  $\text{C}_4\text{H}_4\text{N}_4$ , then reacts with HCN to produce adenine, which is one of purine of DNA and RNA nucleobases (Vasconcelos et al. 2020). Additionally, NCCN is the simplest member of the series of dicyanopolyne,  $(\text{N}\equiv\text{C}-(\text{C}\equiv\text{C})_n-\text{C}\equiv\text{N})$ , which are believed to be potentially abundant interstellar molecules (Kotos & Grabowski 2000; Petrie et al. 2003). However, NCCN is non-polar molecule and cannot be directly observed. Its presence in interstellar space was indirectly detected for the first time through the detection of the protonated form ( $\text{NCCNH}^+$ ) in the dense clouds L483 and TMC-1 (Agúndez et al. 2015). That was further confirmed by the detection of the metastable and polar isomer, isocyanogen (CNCN) (Agúndez et al. 2018). The fractional abundances of  $\text{NCCNH}^+$  and CNCN in L483 and TMC-1 are fairly low, ranging from  $(1 - 10) \times 10^{-12}$  and  $(5 - 9) \times 10^{-11}$ , respectively (Agúndez et al. 2015, 2018). Agúndez et al. (2018) suggested that NCCN could be fairly abundant, with an abundance in dark clouds ranging from  $10^{-9} - 10^{-7}$ . In our hot core models, the peak abundances of NCCN, CNCN and

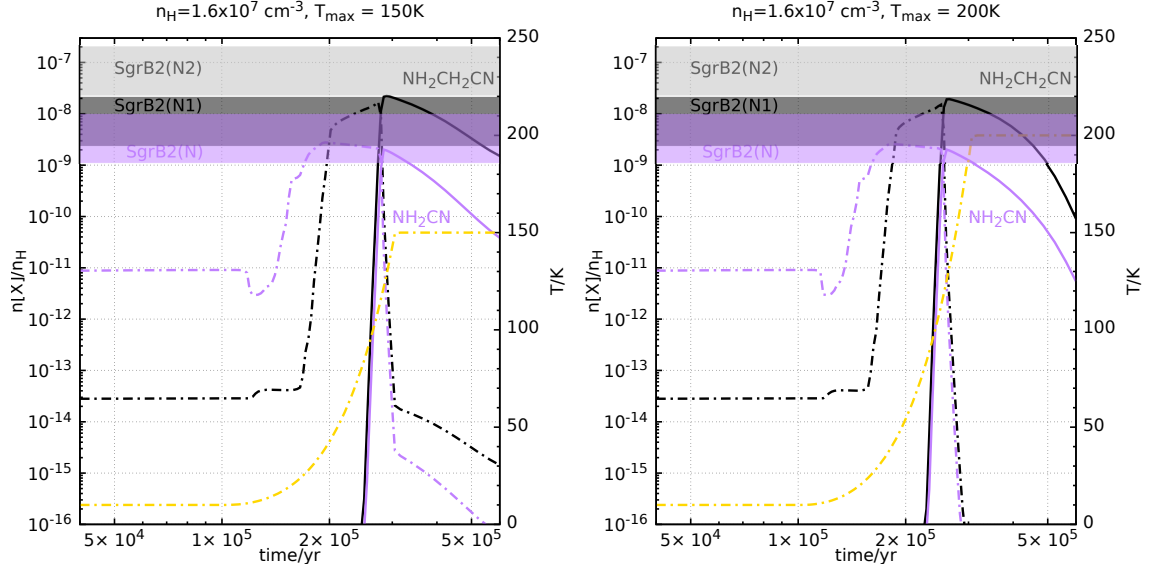


**Figure 6.** The calculated abundances of AAN and  $\text{NH}_2\text{CN}$  in the gas phase and on grain mantles, including surface and icy mantle, are plotted versus time for warm-up stages in hot core models. The density is  $1.6 \times 10^7 \text{ cm}^{-3}$ , and the temperatures remain at a constant value of 10 K. During the warm-up stage,  $T_{\text{max}} = 150 \text{ K}$ ,  $200 \text{ K}$ . Solid lines correspond to the gas phase abundances, dotted lines indicate abundances on the grain mantles. The gray, light gray and purple rectangles represent the observed abundance with  $\pm$  a factor of 3 uncertainty for AAN in Sgr B2(N1) and Sgr B2(N2) and for  $\text{NH}_2\text{CN}$  in Sgr B2(N), respectively. Golden dotted lines denote temperature profiles.

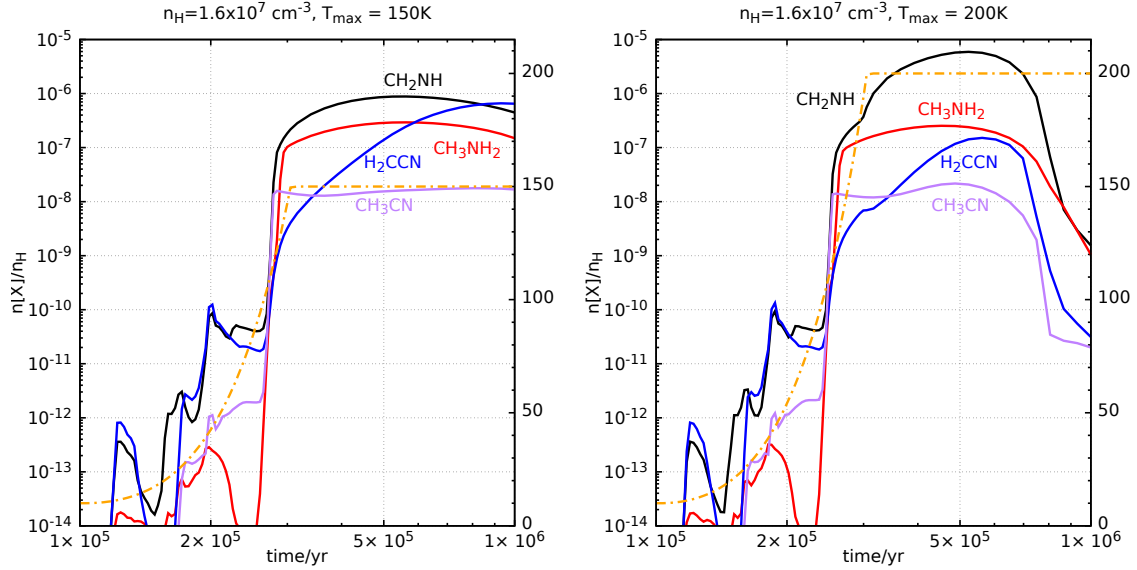


**Figure 7.** The calculated abundances of  $\text{CH}_2\text{NH}$ ,  $\text{CH}_3\text{NH}_2$ ,  $\text{H}_2\text{CCN}$  and  $\text{CH}_3\text{CN}$  in the gas phase are plotted versus time for warm-up stages in hot core models. The density is  $1.6 \times 10^7 \text{ cm}^{-3}$ , and the temperatures remain at a constant value of 10 K. During the warm-up stage,  $T_{\text{max}} = 150$  and  $200 \text{ K}$ . Solid lines correspond to the gas phase abundances of  $\text{CH}_2\text{NH}$ ,  $\text{CH}_3\text{NH}_2$ ,  $\text{H}_2\text{CCN}$  and  $\text{CH}_3\text{CN}$ , Dotted lines denote temperature profiles.

$\text{NCCNH}^+$  can reach  $4.38 \times 10^{-9}$ ,  $3.50 \times 10^{-10}$  and  $1.96 \times 10^{-13}$ , respectively, as shown in Fig. 8. The simulated ratio of  $\text{NCCNH}^+$  to  $\text{NCCN}$  is  $9.25 \times 10^{-5}$ , with  $\text{NCCNH}^+$  reaching its peak abundance at the time of  $2.05 \times 10^6 \text{ yr}$ . These results are consistent with the chemical models predicted by Agúndez et al. (2015). The major formation pathways of  $\text{NCCN}$  involve the reactions of  $\text{CN} + \text{HNC}$ ,  $\text{N} + \text{C}_3\text{N}$  in the gas phase. In the future,  $\text{NCCN}$  could potentially be indirectly observed by detecting the  $\text{NCCNH}^+$  ion, or inferred by detecting its higher-energy polar isomer,  $\text{CNCN}$ , in hot cores. Based on our model results, it is possible that  $\text{NCCN}$  and AAN react to

form  $\text{C}_4\text{H}_4\text{N}_4$ , as they have relatively high abundances in hot core models. However, the reaction need to be verified through theoretical calculations or laboratory experiments. Here we only show the results for a temperature of  $T_{\text{max}} = 150 \text{ K}$ , as  $T_{\text{max}} = 200 \text{ K}$  shows a similar trend.

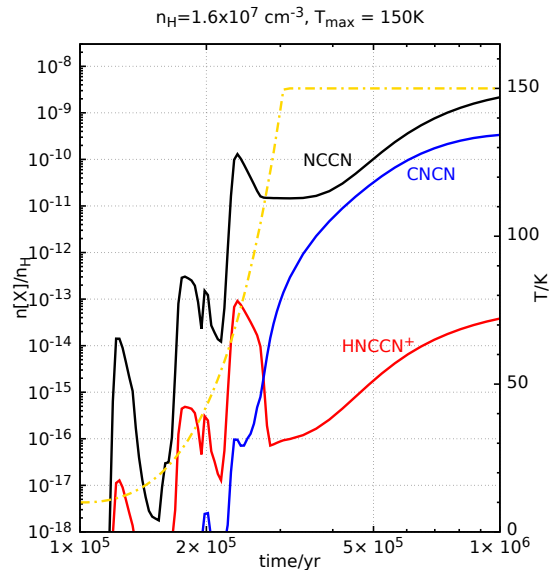


**Figure 8.** The calculated abundances of NCCN, CNCN and NCCNH<sup>+</sup> in the gas phase are plotted versus time for warm-up stages in hot core models. The density is  $1.6 \times 10^7 \text{ cm}^{-3}$ , and the temperatures remain at a constant value of 10 K. During the warm-up stage,  $T_{\text{max}} = 150 \text{ K}$ . Solid lines correspond to the gas phase abundances of NCCN, CNCN and NCCNH<sup>+</sup>, Dotted lines denote temperature profiles.

## 5 CONCLUSIONS

In this work, we conducted chemical simulations to calculate the evolution of  $\text{NH}_2\text{CH}_2\text{CN}$  and its isomers in the ISM. The main results can be summarized as follows:

1. With the updated gas-grain chemical network of the related species along with AAN, our models predicted a peak gas phase abundance of AAN on the order of  $10^{-8}$ , which is consistent with observations towards Sgr B2(N).

2. Our modeling results suggested the formation processes of AAN and its isomers. We found that AAN is formed on grains through the reaction of  $\text{NH}_2 + \text{H}_2\text{CCN}$ ,  $\text{HNC} + \text{CH}_2\text{NH}$  and  $\text{NHCH}_2\text{CN} + \text{H}$  at early evolutionary stages. Subsequently, it thermally evaporates into the gas phase when temperature reaches 100 K and destroyed by positive ions (e.g.,  $\text{H}^+$ ,  $\text{H}_3^+$ ) and free radical OH in the gas phase. Its isomer MCA and MCI are formed through the hydrogenation reaction of  $\text{CH}_3\text{NCN}$  on the grain surfaces and the electron recombination reactions of the ion  $\text{C}_2\text{H}_5\text{N}_2^+$  in the gas phase.

3. Strong UV radiation had minimal effect on the abundances of AAN and MCA, resulting in changes of no more than one order of magnitude. This finding confirms that species containing nitriles survive longer than the corresponding acids when exposed to UV photolysis in the solid state.

4. AAN and  $\text{NH}_2\text{CN}$  are members of the amino nitriles family, as they contain both an amino and a nitrile functional group. They have similar formation processes, occurring through formation on grain surfaces and subsequent thermal evaporation into the gas phase. The ratio of  $\text{NH}_2\text{CN}$  to AAN is 0.1, which is close to the observed value of 0.53.

5. NCCN, the simplest member of the dicyanopolyyne series, can be formed through reactions of  $\text{CN} + \text{HNC}$ ,  $\text{N} + \text{C}_3\text{N}$  in the gas phase. Our models show that its abundance can reach the order of  $10^{-9}$ . Therefore, it is possible that NCCN and AAN react with each other to eventually form adenine in hot cores. This process should be investigated through theoretical calculations or laboratory experiments to understand the validity of grain surface formation of adenine in future work.

## ACKNOWLEDGEMENTS

This work was supported by the National Natural Science Foundation of China under grant 12203091, 12373026, 12173075, the Natural Science Foundation of Xinjiang Uygur Autonomous Region (2022D01A156), the "Tianchi Doctoral Program 2021", the National Key R&D Program of China (No.2022YFA1603103), Youth Innovation Promotion Association CAS.

## DATA AVAILABILITY

The datasets generated during this study are available in the article and from the corresponding author upon request.

## REFERENCES

- Agúndez M., et al., 2015, *A&A*, **579**, L10  
 Agúndez M., Marcelino N., Cernicharo J., 2018, *ApJL*, **861**, L22  
 Bak Børge; Svanholt H., 1980, *ACTA CHEM. SCAND.*, SER. A, **34**, 57  
 Basiuk V. A., 2001, *J.Phys.Chem.A*, **105**, 4252  
 Belloche A., Menten K. M., Comito C., Müller H. S. P., Schilke P., Ott J., Thorwirth S., Hieret C., 2008, *A&A*, **482**, 179  
 Belloche A., Garrod R. T., Müller H. S. P., Menten K. M., Comito C., Schilke P., 2009, *A&A*, **499**, 215  
 Belloche A., Müller H. S. P., Menten K. M., Schilke P., Comito C., 2013, *A&A*, **559**, A47  
 Belloche A., Garrod R. T., Müller H. S. P., Menten K. M., 2014, *Science*, **345**, 1584  
 Bernstein M. P., Ashbourn S. F. M., Sandford S. A., Allamandola L. J., 2004, *ApJ*, **601**, 365  
 Bonfand M., Belloche A., Menten K. M., Garrod R. T., Müller H. S. P., 2017, *A&A*, **604**, A60  
 Bonfand M., Belloche A., Garrod R. T., Menten K. M., Willis E., Stéphan G., Müller H. S. P., 2019, *A&A*, **628**, A27  
 Borget F., Danger G., Duvernay F., Chomat M., Vinogradoff V., Theulé P., Chiavassa T., 2012, *A&A*, **541**, A114  
 Bossa J. B., Duvernay F., Theulé P., Borget F., D'Hendecourt L., Chiavassa T., 2009, *A&A*, **506**, 601

- Choe J. C., 2023, *Phys. Chem. Chem. Phys. (Incor. Faraday Trans.)*, **25**, 16001
- Cleaves H. J. J., 2011, *Aminonitrile*. Springer Berlin Heidelberg, Berlin, Heidelberg, pp 39–40
- Coutens A., et al., 2018, *A&A*, **612**, A107
- Danger G., Bossa J. B., de Marcellus P., Borget F., Duverney F., Theulé P., Chiavassa T., D'Hendecourt L., 2011, *A&A*, **525**, A30
- Das A., Sil M., Gorai P., Chakrabarti S. K., Loison J. C., 2018, *ApJS*, **237**, 9
- Das A., Gorai P., Chakrabarti S. K., 2019, *A&A*, **628**, A73
- Dickens J. E., Irvine W. M., DeVries C. H., Ohishi M., 1997, *ApJ*, **479**, 307
- Dickerson R. E., 1978, *Scientific American*, **239**, 70
- Elsila J. E., Glavin D. P., Dworkin J. P., 2009, *Meteoritics & Planetary Science*, **44**, 1323
- Frisch M. J., et al., 2016, *Gaussian 16*, Revision C.01. Gaussian, Inc., Wallingford, CT, USA
- Fukui K., 1981, *Account. Chem. Res.*, **14**, 363
- Garrod R. T., 2013, *ApJ*, **765**, 60
- Garrod R. T., Herbst E., 2006, *A&A*, **457**, 927
- Garrod R. T., Wakelam V., Herbst E., 2007, *A&A*, **467**, 1103
- Garrod R. T., Belloche A., Müller H. S. P., Menten K. M., 2017, *A&A*, **601**, A48
- Glavin D. P., et al., 2010, *Meteoritics & Planetary Science*, **45**, 1695
- Godfrey P. D., Brown R. D., Robinson B. J., Sinclair M. W., 1973, *Astrophys. Lett.*, **13**, 119
- Goerigk L., Grimme S., 2011, *J. Chem. Theor. Comput.*, **7**, 291
- Graedel T. E., Langer W. D., Frerking M. A., 1982, *ApJS*, **48**, 321
- Grimme S., 2006, *J. Chem. Phys.*, **124**, 034108
- Grimme S., Ehrlich S., Goerigk L., 2011, *J. Comput. Chem.*, **32**, 1456
- Halfen D. T., Ilyushin V. V., Ziurys L. M., 2013, *ApJ*, **767**, 66
- Hasegawa T. I., Herbst E., Leung C. M., 1992, *ApJS*, **82**, 167
- Hassel G. E., Herbst E., Garrod R. T., 2008, *ApJ*, **681**, 1385
- Hoyle F., 1976, *Nature*, **264**, 45
- Koch D. M., Toubin C., Peslherbe G. H., Hynes J. T., 2008, *J. Phys. Chem. C*, **112**, 2972
- Kotos R., Grabowski Z. R., 2000, *Ap&SS*, **271**, 65
- Lattalais M., Pauzat F., Ellinger Y., Ceccarelli C., 2010, *A&A*, **519**, A30
- Lattalais M., Pauzat F., Pilmé J., Ellinger Y., Ceccarelli C., 2011, *A&A*, **532**, A39
- Lee C.-W., Kim J.-K., Moon E.-S., Minh Y. C., Kang H., 2009, *ApJ*, **697**, 428
- Loison J.-C., Wakelam V., Hickson K. M., 2014, *MNRAS*, **443**, 398
- Manna A., Pal S., 2022, *Life Sciences and Space Research*, **34**, 9
- McGuire B. A., Carroll P. B., Loomis R. A., Finneran I. A., Jewell P. R., Remijan A. J., Blake G. A., 2016, *Science*, **352**, 1449
- Melosso M., et al., 2020, *A&A*, **641**, A160
- Merz Kenneth M. J., Aguiar E. C., da Silva J. B. P., 2014, *J. Phys. Chem. A*, **118**, 3637
- Mondal S. K., Iqbal W., Gorai P., Bhat B., Wakelam V., Das A., 2023, *A&A*, **669**, A71
- Öberg K. I., Fuchs G. W., Awad Z., Fraser H. J., Schlemmer S., van Dishoeck E. F., Linnartz H., 2007, *ApJL*, **662**, L23
- Pelc A., Huber S. E., Matias C., Czupyt Z., Denifl S., 2016, *J. Phys. Chem. A*, **120**, 903
- Peltzer E. T., Bada J. L., Schlesinger G., Miller S. L., 1984, *Advances in Space Research*, **4**, 69
- Petrie S., Millar T. J., Markwick A. J., 2003, *MNRAS*, **341**, 609
- Purvis III G. D., Bartlett R. J., 1982, *J. Chem. Phys.*, **76**, 1910
- Puzzarini C., Salta Z., Tasinato N., Lupi J., Cavallotti C., Barone V., 2020, *MNRAS*, **496**, 4298
- Qin S.-L., Wu Y., Huang M., Zhao G., Li D., Wang J.-J., Chen S., 2010, *ApJ*, **711**, 399
- Quan D., Herbst E., 2007, *A&A*, **474**, 521
- Quan D., Herbst E., Osamura Y., Roueff E., 2010, *ApJ*, **725**, 2101
- Quan D., Herbst E., Corby J. F., Durr A., Hassel G., 2016, *ApJ*, **824**, 129
- Richard C., Belloche A., Margulès L., Motiyenko R. A., Menten K. M., Garrod R. T., Müller H. S. P., 2018, *JMoSp*, **345**, 51
- Ruud M., Loison J. C., Hickson K. M., Gratier P., Hersant F., Wakelam V., 2015, *MNRAS*, **447**, 4004
- Ruud M., Wakelam V., Hersant F., 2016, *MNRAS*, **459**, 3756
- San Andrés D., et al., 2024, *ApJ*, **967**, 39
- Scuseria G. E., Schaefer III H. F., 1989, *J. Chem. Phys.*, **90**, 3700
- Scuseria G. E., Janssen C. L., Schaefer Iii H. F., 1988, *J. Chem. Phys.*, **89**, 7382
- Semenov D., et al., 2010, *A&A*, **522**, A42
- Shingledecker C. N., Molpeceres G., Rivilla V. M., Majumdar L., Kästner J., 2020, *ApJ*, **897**, 158
- Sleiman C., El Dib G., Rosi M., Skouteris D., Balucani N., Canosa A., 2018, *Phys. Chem. Chem. Phys. (Incor. Faraday Trans.)*, **20**, 5478
- Su T., Chesnavich W. J., 1982, *J. Chem. Phys.*, **76**, 5183
- Suzuki T., Ohishi M., Hirota T., Saito M., Majumdar L., Wakelam V., 2016, *ApJ*, **825**, 79
- Vasconcelos F. A., Pilling S., Agnihotri A., Rothard H., Boduch P., 2020, *Icarus*, **351**, 113944
- Wakelam V., et al., 2015, *ApJS*, **217**, 20
- Wang Y., Pan J.-A., Wu H., Talapin D. V., 2019, *ACS Nano*, **13**, 13917
- Wirström E. S., Bergman P., Hjalmarson Å., Nummelin A., 2007, *A&A*, **473**, 177
- Woon D. E., 2002, *ApJ*, **571**, L177
- Woon D. E., Herbst E., 2009, *ApJS*, **185**, 273
- Xu S., Wang N., 2007, *Acta Physico-Chimica Sinica*, **23**, 212
- Zhang X., Quan D., Chang Q., Herbst E., Esimbek J., Webb M., 2020, *MNRAS*, **497**, 609
- Zhang X., Quan D., Li R., Esimbek J., Chen L.-F., Zhao G., Zhou Y., 2023, *MNRAS*, **521**, 1578

This paper has been typeset from a  $\text{\TeX}/\text{\LaTeX}$  file prepared by the author.